Supporting Information

Processing natural wood into an efficient and durable solar steam generation device

Ning Ma,‡ Qiang Fu,‡ Yuexian Hong, Xuyang Hao, Xiaoge Wang, Jing Ju, Junliang Sun**

College of Chemistry and Molecular Engineering, Peking University, Beijing National Laboratory for Molecular Sciences (BNLMS), Beijing, 100871, People's Republic of China.

Keywords: solar steam generator, wood, MXene, chemical process, durability.

Corresponding Author: junliang.sun@pku.edu.cn; jingju@pku.edu.cn
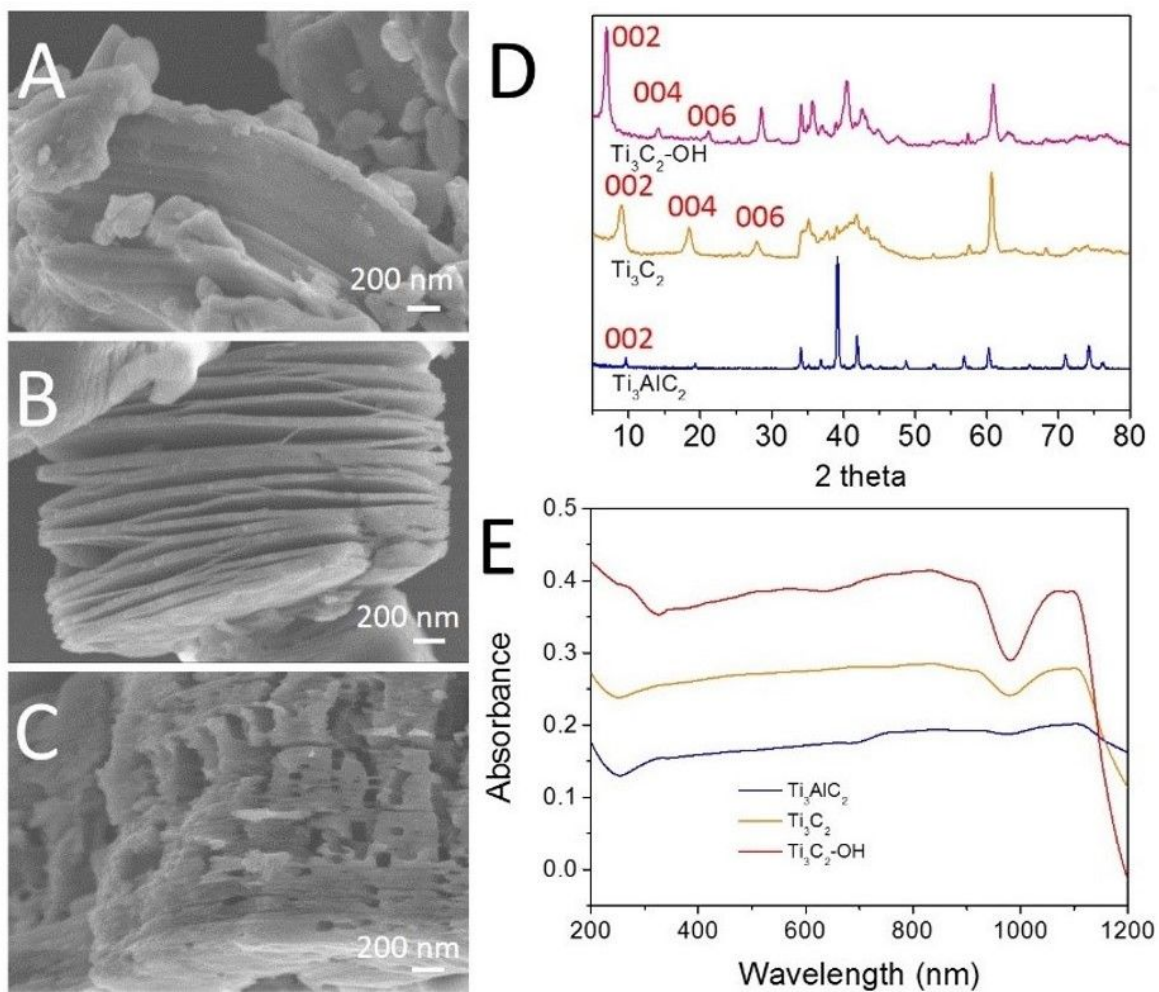
Figure S1. Photothermal conversion efficiency and mechanism. SEM images of A) Ti_3AlC_2, B) Ti_3C_2, C) Ti_3C_2-OH; D) PXRD of Ti_3AlC_2, Ti_3C_2 and Ti_3C_2-OH; E) UV/Vis spectra of Ti_3AlC_2, Ti_3C_2 and Ti_3C_2-OH.
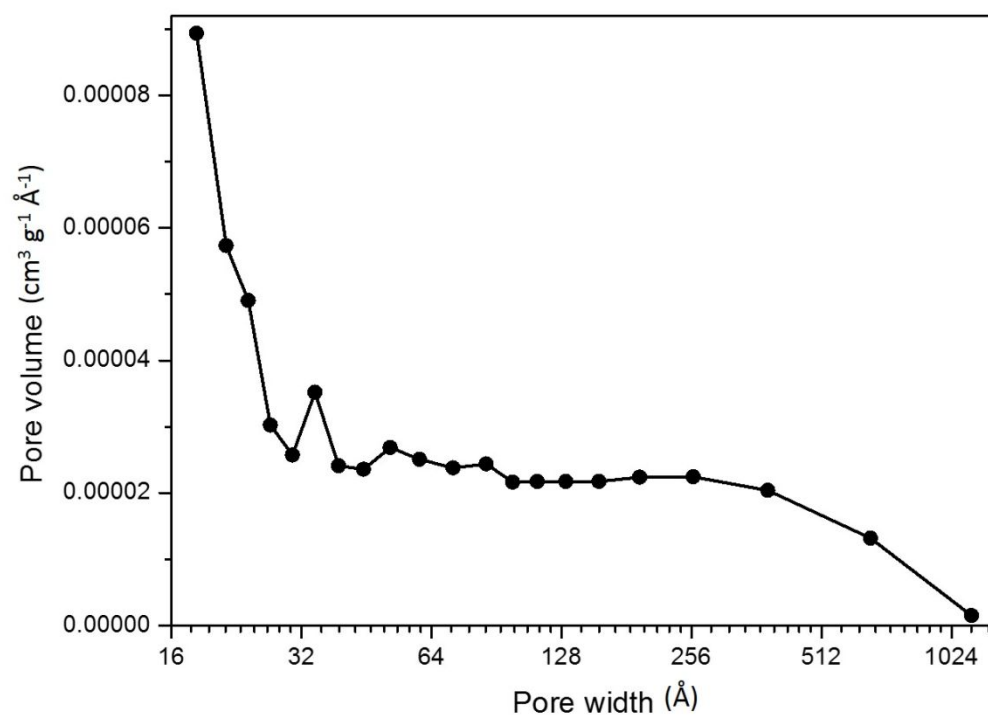
Figure S2. BJH Desorption dV/dw Pore Volume of Ti$_3$C$_2$-OH. The pore size existing in Ti$_3$C$_2$-OH, carefully examined by Brunauer−Emmett−Teller (BET) test, is about 40 nm, due to defect-etching strategy.
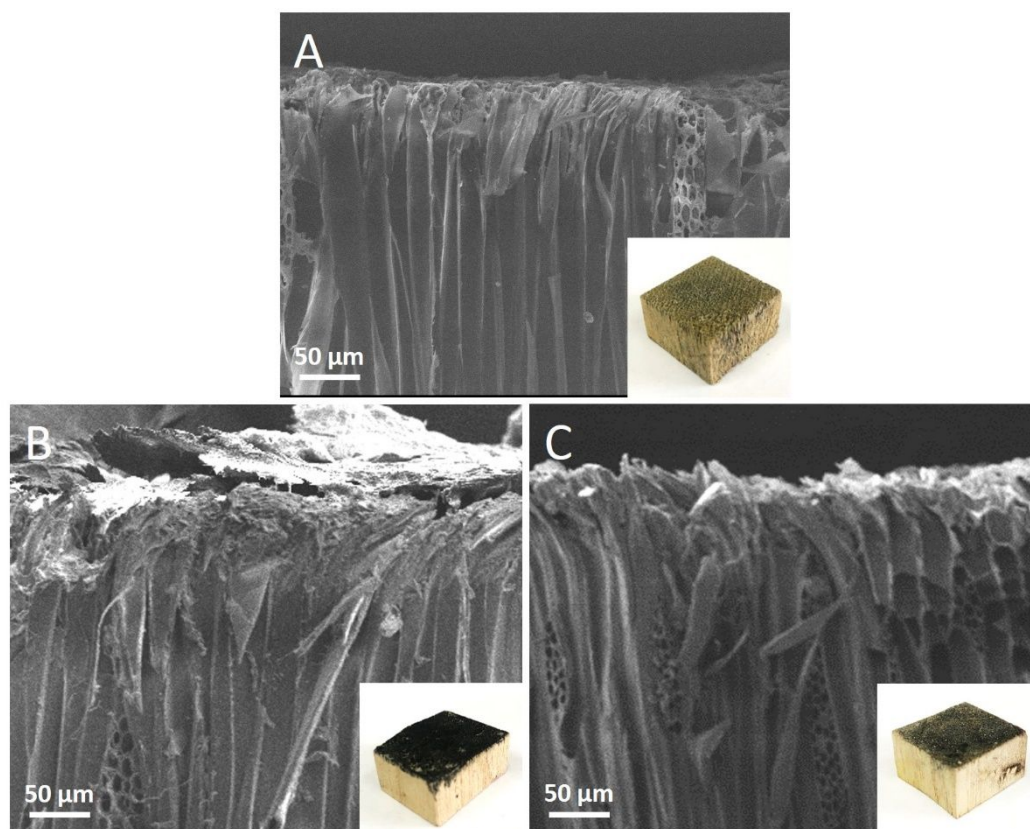
Figure S3. SEM observation on the three physical method combined materials: A) SEM image of Ti_3C_2-Phys -wood; B) SEM image of GO-Phys-wood; C) SEM image of AC-Phys-wood. It is hard for Ti_3C_2 and AC to stay on the surface of the wood. It can be in form of GO film on the surface of wood, accompanying with peeled off.
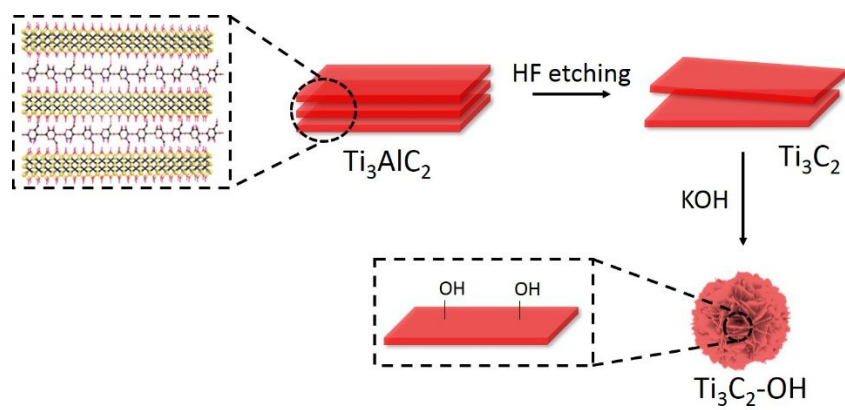
Figure S4. Preparation of Ti$_3$C$_2$-OH
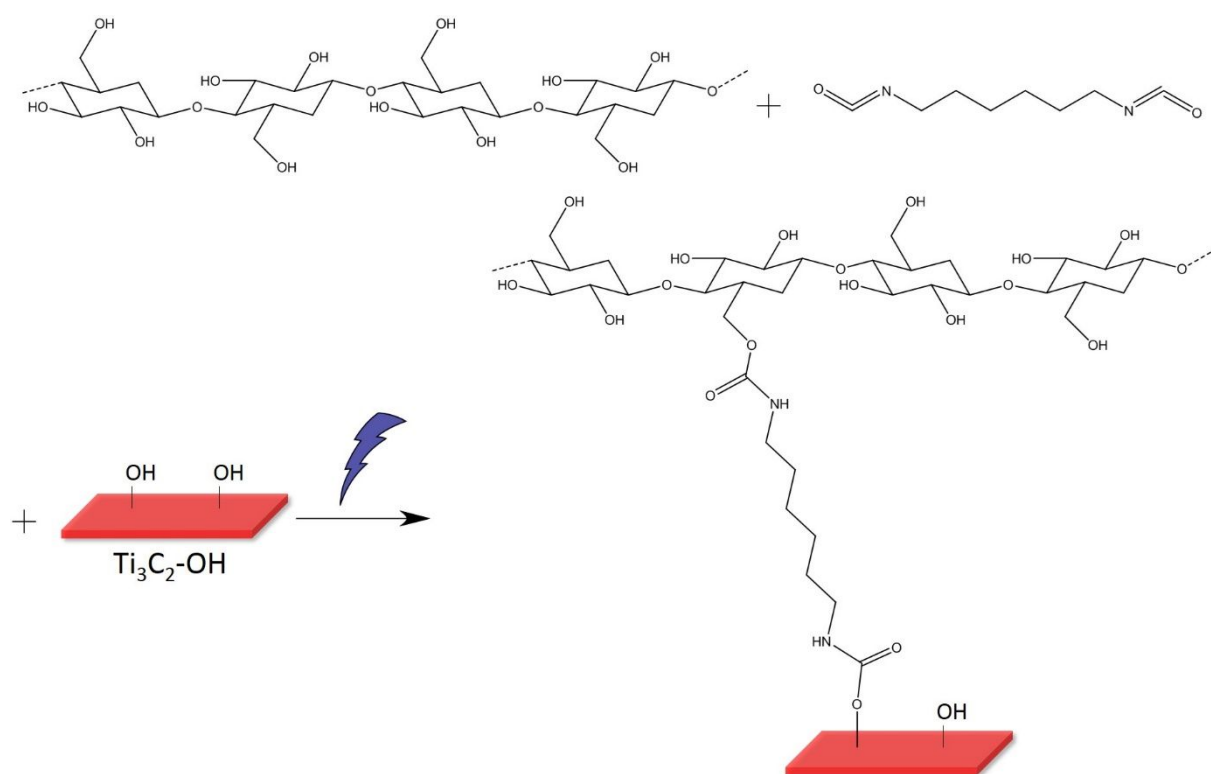
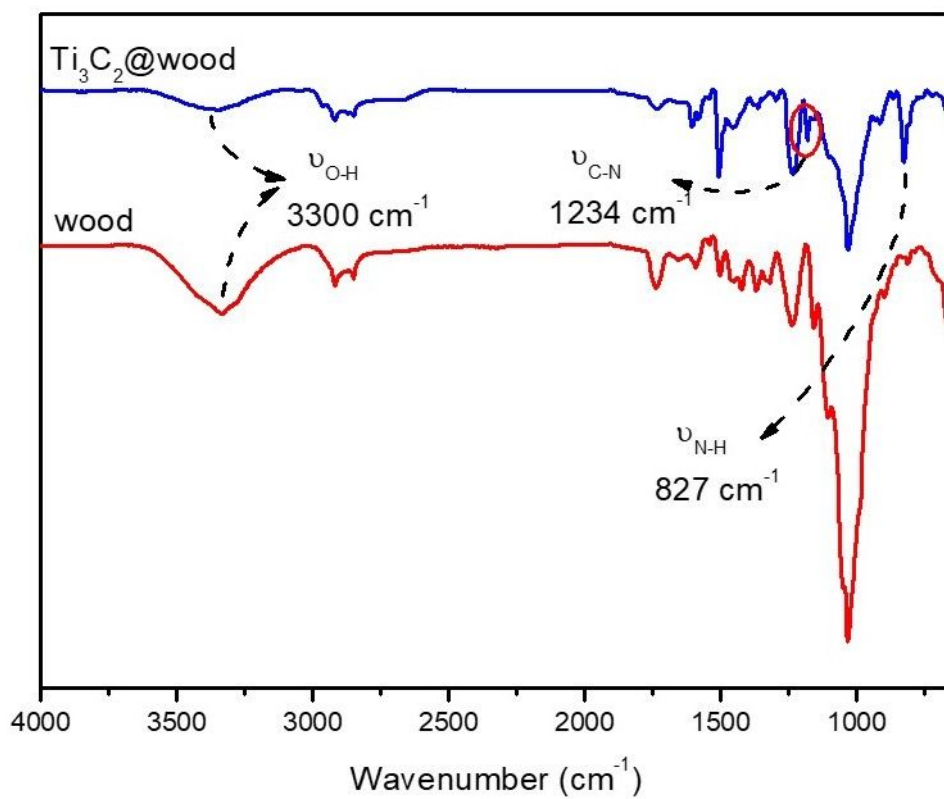**Figure S5.** Chemical reaction of Ti$_3$C$_2$-OH and wood.

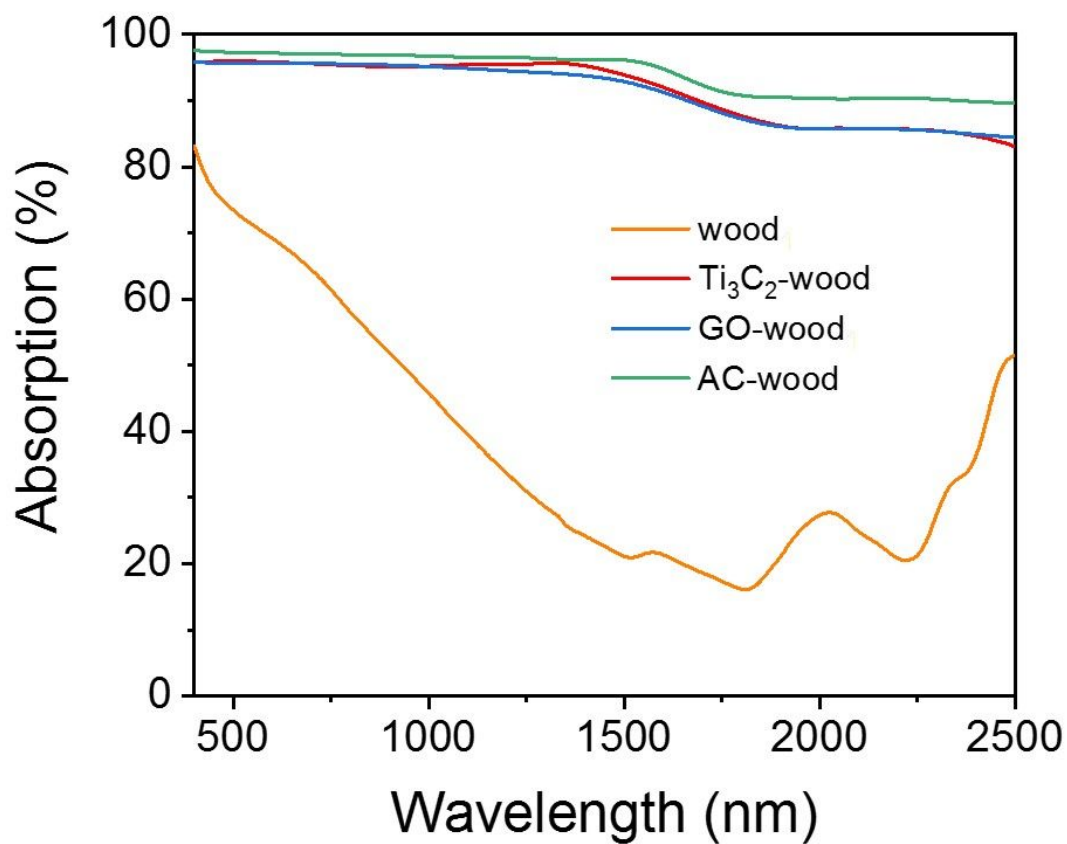**Figure S6.** FT-IR spectra of wood and Ti_3C_2-wood.

Figure S7. Experimentally measured light absorption spectra for Ti_3C_2-wood, GO-wood, AC-wood and natural wood. The bilayer wood absorbs nearly all the incident light over the entire wavelength range due to synergistic effects between the wood's microstructure and Ti_3C_2 layer composition.

Following Jurin's Law[1-3], this height can be obtained by balancing the weight of the liquid that has ascended in these channels with the surface tension force experienced by the ascended liquid column. The equilibrium height to which water will rise within the Paulownia wood block was:

$$h = \frac{2\gamma \sum_{i=1}^{k} x_i R_i}{\rho_w g \sum_{i=1}^{k} x_i R_i^2} \qquad (1)$$

In the above equation, γ is the water surface tension 72.75×10^{-3} N/m and ρ_w is the density of water. Here is a total of N number of channels of k different radii (R1, R2.... Rk). The number of each channel is n1, n2.... nk, respectively. Therefore, the number density of the channels can be denoted as x1, x2.... xk (where xj=nj/N).
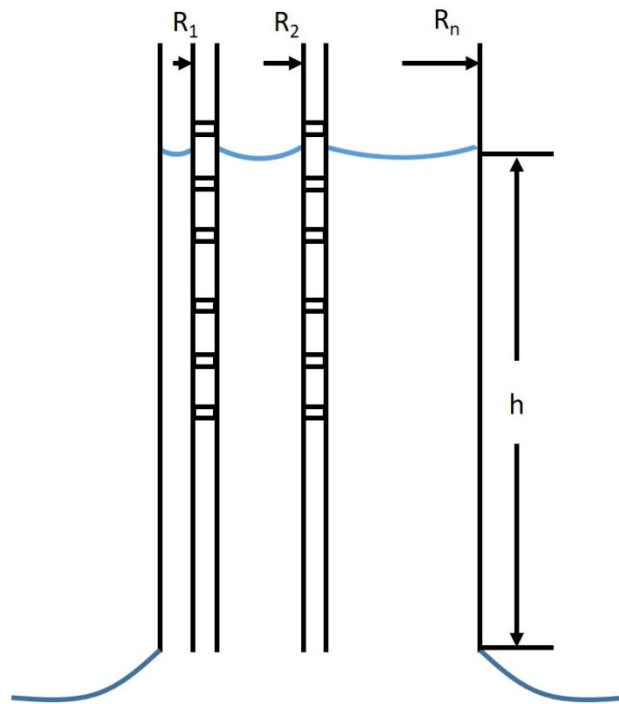
For this project, Table S1 provides the distribution of Paulownia wood microcapillaries as show in Figure 2I.

Table S1 Distribution of radii for the Paulownia wood channels.

R(μm)	Frequency(ni)	Xi=ni/N
5	211	0.2414
10	372	0.4256
15	236	0.2700
20	47	0.0538
25	5	0.0057
60	2	0.0023
70	1	0.0011

These values in Table S1 were plugged into Eq. (1) to obtain the equilibrium height:
h=1.097 m.

According to the Jurin's Law, the equilibrium height is 21.2 cm, if $R_1=R_2=\ldots R_n=70\mu m$. And, if $R_1=R_2=\ldots R_n=60\mu m$, the equilibrium height is 24.7 cm.

Besides, if the radii are narrow overall, the water flow rate of the unit surface will be slow down.[4]

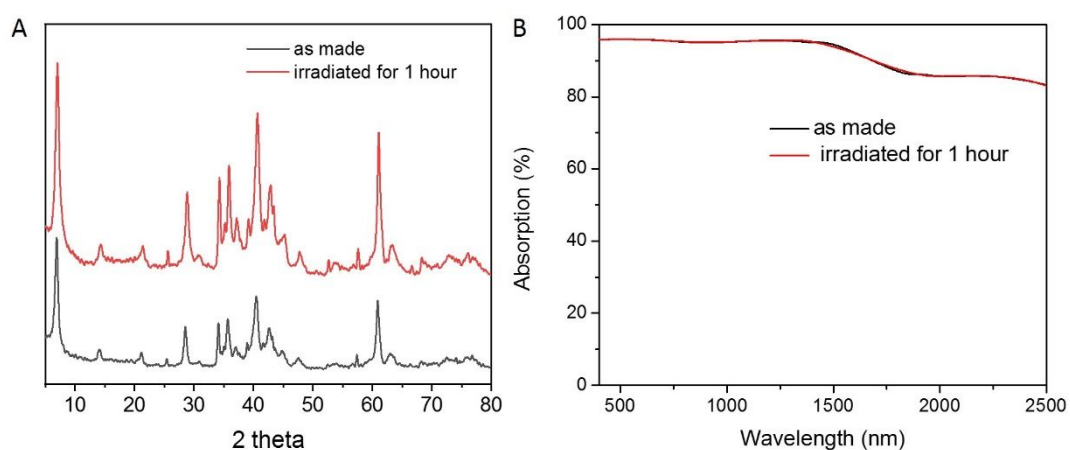**Figure S8.** To illustrate the solar thermal stability of Ti_3C_2-OH, we analyzed the PXRD pattern and UV-Vis after irradiated under 1 sun. A) PXRD pattern and B) UV-Vis spectra of Ti_3C_2-OH before and after one-hour irradiation.

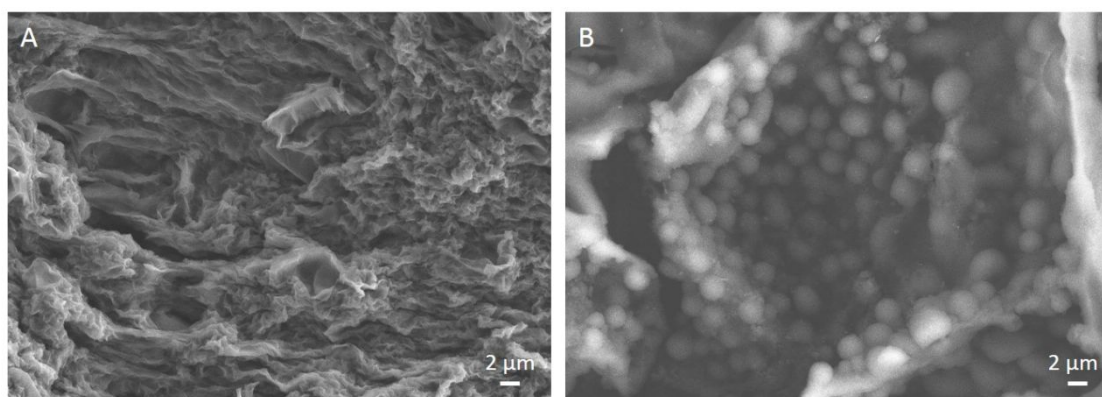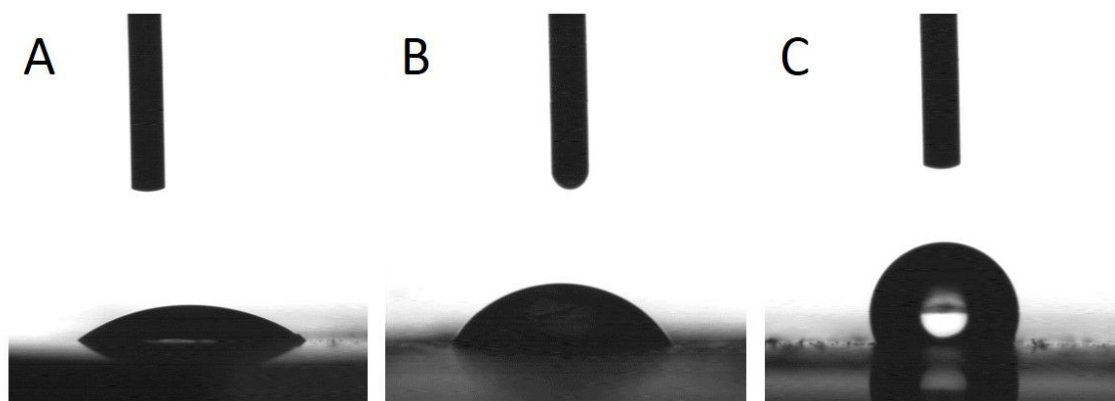**Figure S9.** SEM images of A) GO and B) AC.

Figure S10. Contact angles of A) Ti_3C_2, B) GO and C) AC. The wettability of these three materials was characterized by water contact angle so as to understand the differences in the intrinsic water generation performance. As shown in the Figure S7, Ti_3C_2, GO, AC show an increasing contact angle from 37.4^o, 48.5^o, to 110.0^o, respectively.

Simulation

The fluid field distribution, as well as the temperature distribution was simulated using the COMSOL Multiphysics finite-element-based solver (http://cn.comsol.com). The simulation of the two-phase flow in the porous media (wood) was modelled using the Brinkman model, in which the capillary effect is treated by an additional diffusion term in the transport equation. The flow field $\boldsymbol{u}_g$ and pressure distribution p_g of wet air in porous media are calculated by using the finite-element-based solver. Therefore, the porosity ε must consider that the gas phase occupies only a small part of the void space. The liquid phase velocity is small compared to the moist air velocity, and such that Darcy's law is defined in terms of the gas phase pressure gradient to calculate the water velocity $\boldsymbol{u}_l$ according to

$$\boldsymbol{u}_l = -\frac{\kappa_l}{\mu_l}\nabla p_g \tag{2}$$

where κ_l and μ_l are the permeability and viscosity of the liquid phase. There is no need to define the second Darcy's law equation, but another liquid transport equation is needed.

The boundary conditions for the flow equations and their coupling is the same as in the corresponding model (see Flow Properties).

The moist air phase diffusion was simulated by using the "Dilute matter transfer" module. The second transfer mechanism is the flux produced by the binary diffusion of water vapor and vapor-phase dry vacancies. The effective diffusion coefficient D_{eff} between these two components can usually be described by the Millington & Quirk equation:

$$D_{eff} = D_{va}\varepsilon^{4/3}S_g^{10/3} \tag{3}$$

with the vapor-air diffusivity $D_{va} = 2.6*10^{-5}$ m^2/s.

Both liquid and gas surroundings provide the velocity field that is applied to the water vapor transport equation:

$$\boldsymbol{u} = \frac{\boldsymbol{u}_g}{s_g\varepsilon} - \frac{M_a D_{eff}}{M_{ma}\rho_{ma}}\nabla\rho_{Ma} \tag{4}$$

M_{ma} and ρ_{ma} refer to the moist air molar mass and density.

In order to calculate the amount of water evaporated into the air, and considering the reduction in liquid water and the increase in the proportion of wet air, the function is used:

$$m_{evap} = K(a_w n_{sat} - n) \tag{5}$$

where K is the evaporation rate, n_{sat} the vapor dosage under saturation conditions and n the current vapor dosage.

The free flow domain contains only wet air, and the velocity field obtained from the laminar flow equation is used to describe convective heat transfer. According to the following formula, heat of evaporation is used as the source term to insert the heat transfer equation:

$$Q = -H_{vap}{\cdot}m_{vap} \tag{6}$$

where H_{vap} is the latent heat of evaporation.

Figure S11. 2D view of simulated fluid field distribution of Ti_3C_2-wood evaporation system.
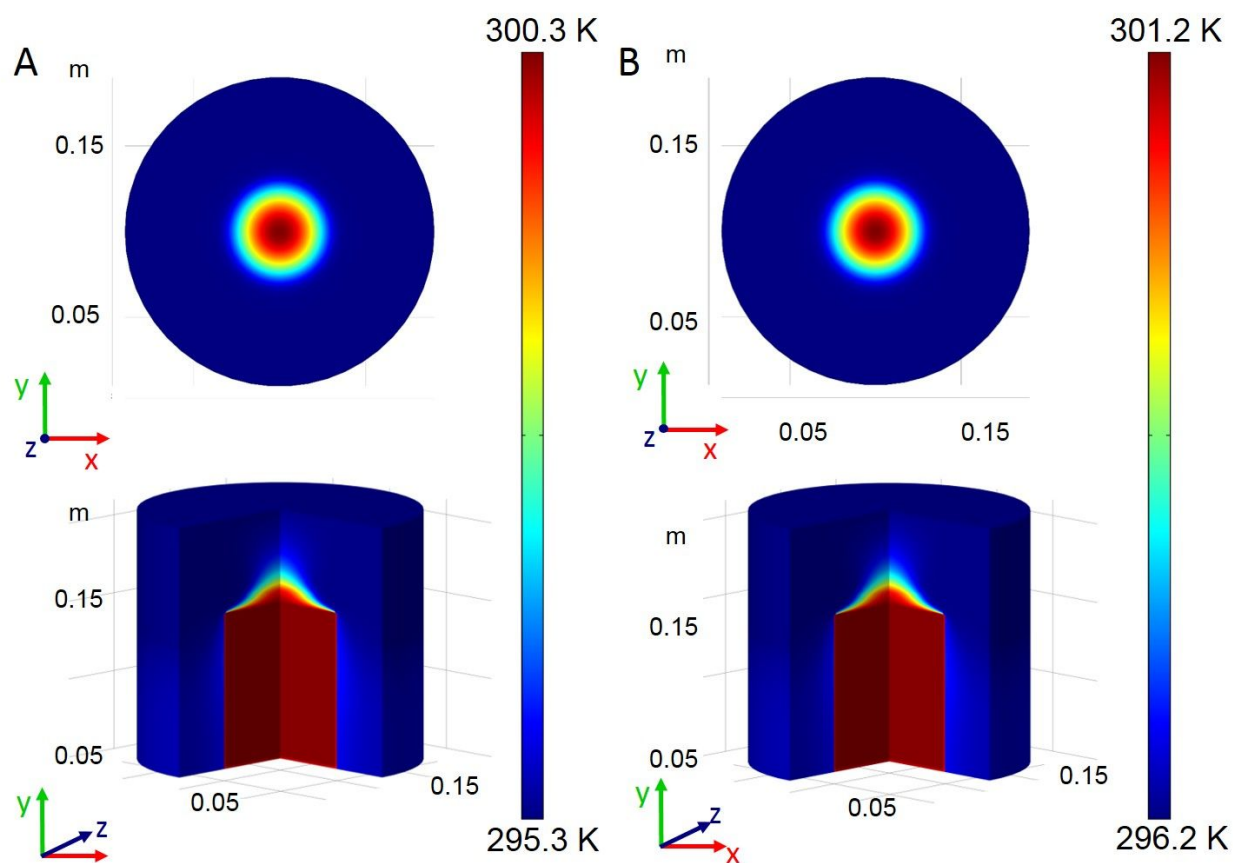
Figure S12. Simulated temperature distribution of Ti_3C_2-wood evaporation system under A) 1 sun and B) 2 suns.
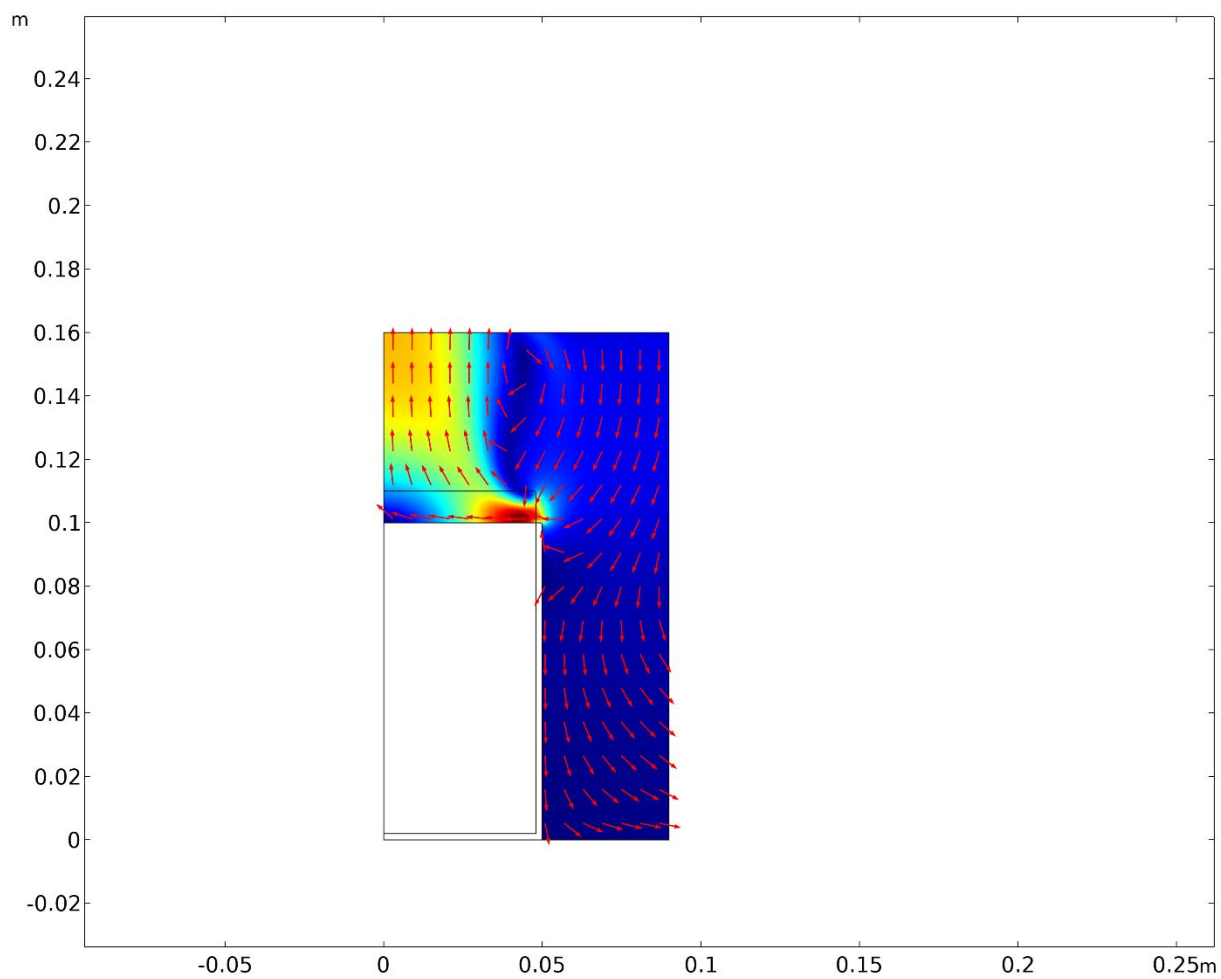
Figure S13. Simulated temperature distribution of GO-wood evaporation system. D) Simulated fluid field distribution of GO-wood evaporation system.
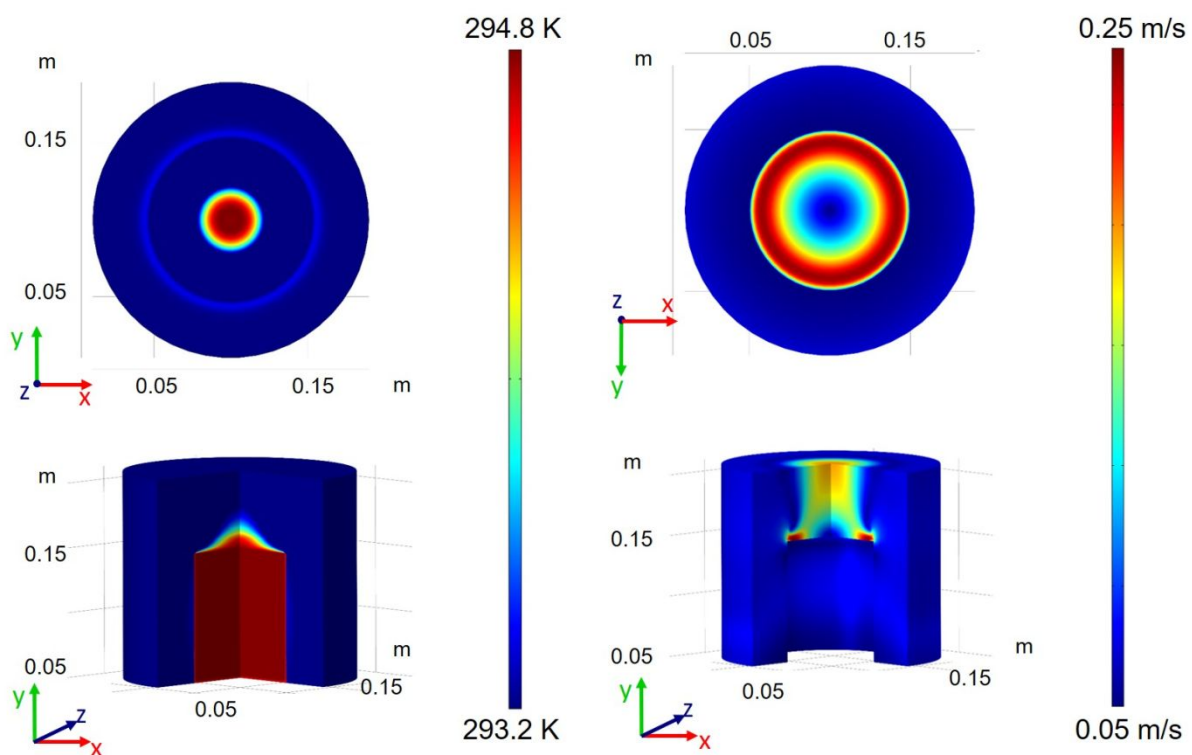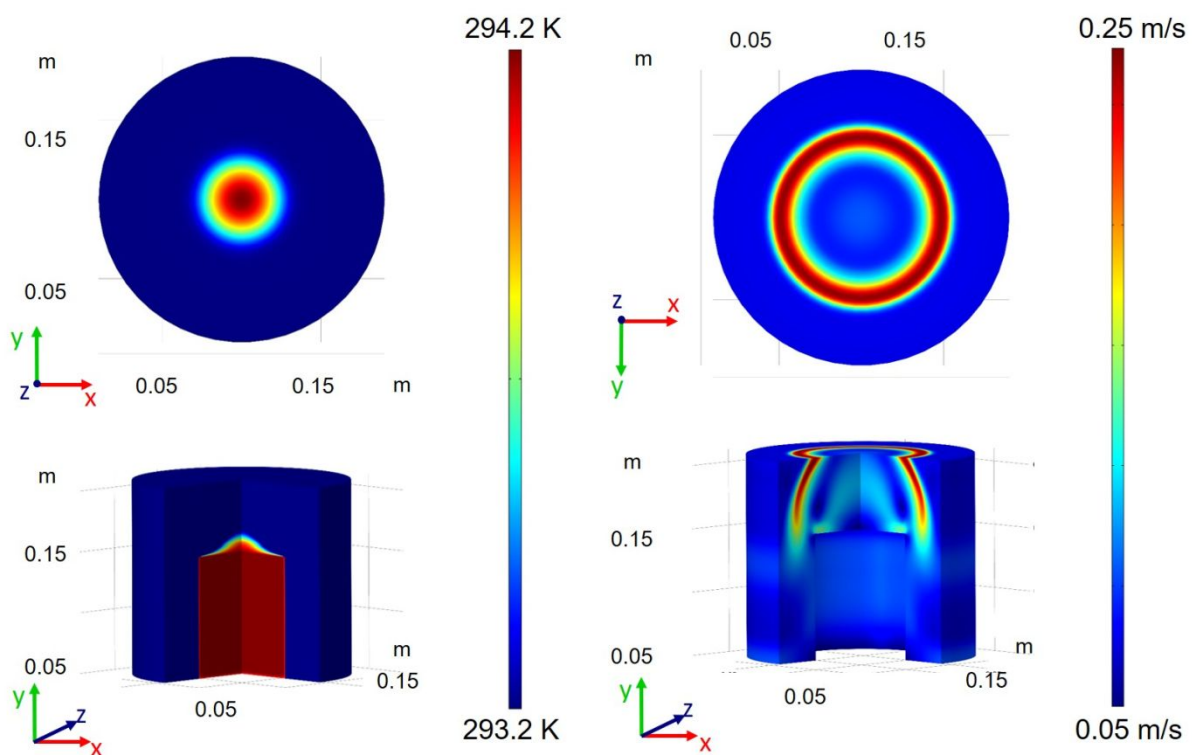
Figure S14. Simulated temperature distribution of AC-wood evaporation system. D) Simulated fluid field distribution of AC-wood evaporation system.
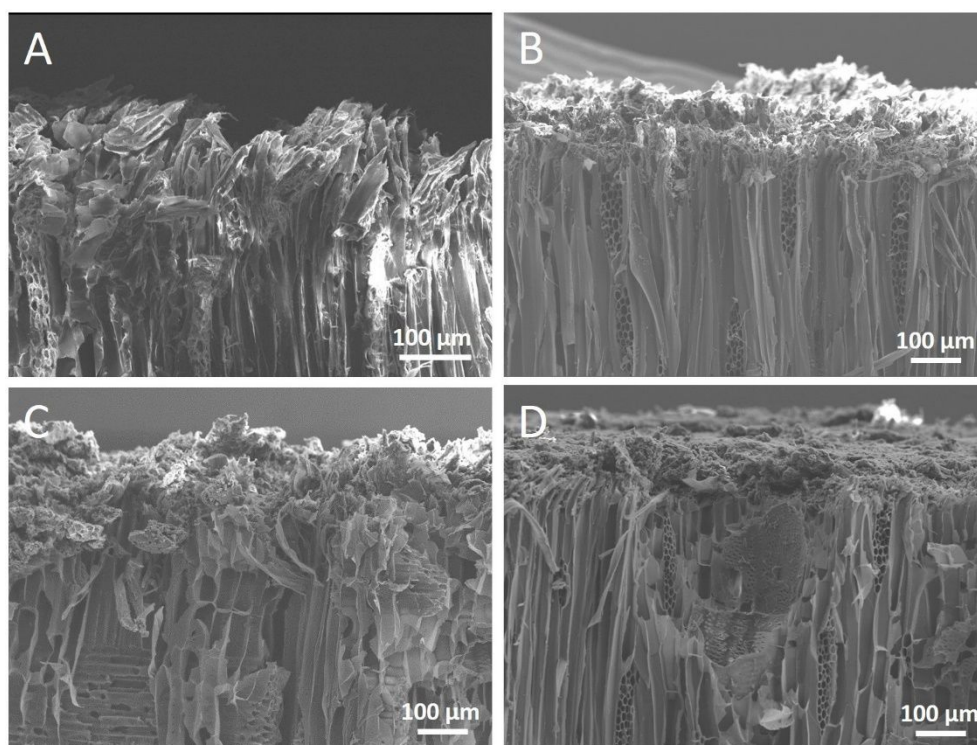
Figure S15. The morphology of A) the wood B) Ti$_3$C$_2$-wood, C) GO-wood, and D) AC-wood after exposed in the outside for two weeks (March 2020).

Table S2 Interfacial water evaporation efficiency based on different types of materials from the selected typical publications.

Materials	Efficiency(%)	Solar intensity (kW m^{-2})	Types	Reference
Ti$_3$C$_2$-wood	96	1	MXene	This work
Al NPs/AAM	88.4/91	4/6	Metal	[5]
Au/Al2O3 template	90	4	Metal	[6]
Au nanoflowers/silica gel	85	1	Metal	[7]
Cup-shaped structure of mixed metal oxide	140	1	Metal oxides	[8]
TiO2−PDA/PPy/cotton	98	1	Metal oxides	[9]
Carbon sponge	90	1	Carbon materials	[10]
Vertically aligned graphene sheets membrane	86.5/94.2	1/4	Carbon materials	[11]
Hierarchical graphene foam	91.4	1-5	Carbon materials	[12]
Plasmonic wood	85	10	Carbon materials	[13]
3D-printed GO-based evaporator	85.6	1	Carbon materials	[14]
Carbonized wood	86.7	10	Carbon materials	[15]
Graphite/wood	80/89	1/10	Carbon materials	[16]
Surface-carbonized longitudinal wood	89	10	Carbon materials	[10]
Carbon black/GO	87.5	1	Carbon materials	[17]
rGO/polyurethane foam	81	10	Carbon materials	[18]
rGO/filter paper	89.2	1	Carbon materials	[19]
GO film/cotton rod	85	1	Carbon materials	[20]
(Bluetec)/PVA/Electrospun PVDF-HFP nanofibers	72	1	Polymers	[21]
Carbon black NPs coated PVDF menbrane	74.6	1.3	Polymers	[22]
Dye modified PTFE membranes	60	1	Polymers	[23]

REFERENCES

1.   Quere, D. Inertial Capillarity. *Europhysics Letters* **1997,** *39*, 533-538.
2.   Zhu, M.; Li, Y.; Chen, G.; Jiang, F.; Yang, Z.; Luo, X.; Wang, Y.; Lacey, S. D.; Dai, J.; Wang, C.; Jia, C.; Wan, J.; Yao, Y.; Gong, A.; Yang, B.; Yu, Z.; Das, S.; Hu, L. Tree-Inspired Design for High-Efficiency Water Extraction *Advanced materials* **2017,** *29*, 1704107.
3.   Das, S.; Waghmare, P. R.; Mitra, S. K. Early Regimes of Capillary Filling *Phys Rev E Stat Nonlin Soft Matter Phys* **2012,** *86*, 067301.
4.   Markicevic, B.; Navaz, H. K. The Influence of Capillary Flow on the Fate of Evaporating Wetted Imprint of the Sessile Droplet in Porous Medium *Physics of Fluids* **2010,** *22*, 122103.
5.   Zhou, L.; Tan, Y.; Wang, J.; Xu, W.; Yuan, Y.; Cai, W.; Zhu, S.; Zhu, J. 3D Self-assembly of Aluminium Nanoparticles for Plasmon-enhanced Solar Desalination *Nature Photonics* **2016,** *10*, 393-398.
6.   Li, X.; Xu, W.; Tang, M.; Zhou, L.; Zhu, B.; Zhu, S.; Zhu, J. Graphene Oxide-based Efficient and Scalable Solar Desalination under One Sun with a Confined 2D Water Path. *Proceedings of the National Academy of Sciences of the United States of America* **2016,** *113*, 13953-13958.
7.   Ding, T.; Zhu, L.; Wang, X.-Q.; Chan, K. H.; Lu, X.; Cheng, Y.; Ho, G. W. Hybrid Photothermal Pyroelectric and Thermogalvanic Generator for Multisituation Low Grade Heat Harvesting *Advanced Energy Materials* **2018,** *8*, 1802397.
8.   Shi, Y.; Li, R.; Jin, Y.; Zhuo, S.; Shi, L.; Chang, J.; Hong, S.; Ng, K.-C.; Wang, P. A 3D Photothermal Structure toward Improved Energy Efficiency in Solar Steam Generation *Joule* **2018,** *2*, 1171-1186.
9.   Hao, D.; Yang, Y.; Xu, B.; Cai, Z., Bifunctional Fabric with Photothermal Effect and Photocatalysis for Highly Efficient Clean Water Generation *ACS Sustainable Chemistry & Engineering* **2018,** *6*, 10789-10797.
10. Liu, H.; Chen, C.; Chen, G.; Kuang, Y.; Zhao, X.; Song, J.; Jia, C.; Xu, X.; Hitz, E.; Xie, H.; Wang, S.; Jiang, F.; Li, T.; Li, Y.; Gong, A.; Yang, R.; Das, S.; Hu, L. High-Performance Solar Steam Device with Layered Channels: Artificial Tree with a Reversed Design *Advanced Energy Materials* **2018,** *8*, 1701616.
11. Zhang, P.; Li, J.; Lv, L.; Zhao, Y.; Qu, L. Vertically Aligned Graphene Sheets Membrane for Highly Efficient Solar Thermal Generation of Clean Water *ACS Nano* **2017,** *11*, 5087-5093.
12. Ren, H.; Tang, M.; Guan, B.; Wang, K.; Yang, J.; Wang, F.; Wang, M.; Shan, J.; Chen, Z.; Wei, D.; Peng, H.; Liu, Z. Hierarchical Graphene Foam for Efficient Omnidirectional Solar-Thermal Energy Conversion *Advanced Materials* **2017,** *29,* 1702590.
13. Zhu, M.; Li, Y.; Chen, F.; Zhu, X.; Dai, J.; Li, Y.; Yang, Z.; Yan, X.; Song, J.; Wang, Y.; Hitz, E.; Luo, W.; Lu, M.; Yang, B.; Hu, L. Plasmonic Wood for High-Efficiency Solar Steam Generation *Advanced Energy Materials* **2018,** *8*, 1701028.
14. Li, Y.; Gao, T.; Yang, Z.; Chen, C.; Luo, W.; Song, J.; Hitz, E.; Jia, C.; Zhou, Y.; Liu, B.; Yang, B.; Hu, L. 3D-Printed, All-in-One Evaporator for High-Efficiency Solar Steam Generation under 1 Sun Illumination *Advanced Materials* **2017,** *29*, 1700981.
15. Jia, C.; Li, Y.; Yang, Z.; Chen, G.; Yao, Y.; Jiang, F.; Kuang, Y.; Pastel, G.; Xie, H.; Yang, B.; Das, S.; Hu, L. Rich Mesostructures Derived from Natural Woods for Solar Steam Generation *Joule* **2017,** *1*, 588-599.

16. Li, T.; Liu, H.; Zhao, X.; Chen, G.; Dai, J.; Pastel, G.; Jia, C.; Chen, C.; Hitz, E.; Siddhartha, D.; Yang, R.; Hu, L. Scalable and Highly Efficient Mesoporous Wood-Based Solar Steam Generation Device: Localized Heat, Rapid Water Transport. *Advanced Functional Materials* **2018,** *28*, 1707134.

17. Li, Y.; Gao, T.; Yang, Z.; Chen, C.; Kuang, Y.; Song, J.; Jia, C.; Hitz, E. M.; Yang, B.; Hu, L. Graphene Oxide-based Evaporator with One-dimensional Water Transport Enabling High-efficiency Solar Desalination *Nano Energy* **2017,** *41*, 201-209.

18. Wang, G.; Fu, Y.; Guo, A.; Mei, T.; Wang, J.; Li, J.; Wang, X. Reduced Graphene Oxide-Polyurethane Nanocomposite Foam as a Reusable Photoreceiver for Efficient Solar Steam Generation *Chemistry of Materials* **2017,** *29*, 5629-5635.

19. Kim, K.; Yu, S.; An, C.; Kim, S.-W.; Jang, J.-H. Mesoporous Three-Dimensional Graphene Networks for Highly Efficient Solar Desalination under 1 sun Illumination *ACS Appl. Mater. Interfaces* **2018,** *10*, 15602-15608.

20. Li, X.; Lin, R.; Ni, G.; Xu, N.; Hu, X.; Zhu, B.; Lv, G.; Li, J.; Zhu, S.; Zhu, J. Three-Dimensional Artificial Transpiration for Efficient Solar Waste-water Treatment *National Science Review* **2018,** *5*, 70-77.

21. Xue, G.; Chen, Q.; Lin, S.; Duan, J.; Yang, P.; Liu, K.; Li, J.; Zhou, J. Highly Efficient Water Harvesting with Optimized Solar Thermal Membrane Distillation Device *Global Challenges* **2018,** *2*, 1800001.

22. Wu, J.; Zodrow, K. R.; Szemraj, P. B.; Li, Q. Photothermal Nanocomposite Membranes for Direct Solar Membrane Distillation. *Journal of Materials Chemistry A* **2017,** *5*, 23712-23719.

23. Fujiwara, M.; Kikuchi, M. Solar Desalination of Seawater using Double-dye-modified PTFE Membrane *Water Research* **2017,** *127*, 96-103.